Plasma Sources Science and Technology

PAPER

Turing patterns on a plasma-liquid interface

IOP Publishing Plasma Sources Science and Technology
Plasma Sources Sci. Technol. **28** (2019) 105014 (7pp) https://doi.org/10.1088/1361-6595/ab45e4

Turing patterns on a plasma-liquid interface

Paul Rumbach[1,4], **Alan E Lindsay**[2] and **David B Go**[1,3]

[1] Department of Aerospace and Mechanical Engineering, University of Notre Dame, Notre Dame, IN 46556, United States of America
[2] Department of Applied & Computational Mathematics & Statistics, University of Notre Dame, Notre Dame, IN 46556, United States of America
[3] Department of Chemical and Biomolecular Engineering, University of Notre Dame, Notre Dame, IN 46556, United States of America

E-mail: prumbach@nd.edu

Received 14 June 2019, revised 26 August 2019
Accepted for publication 18 September 2019
Published 21 October 2019

Abstract

Radially symmetric patterns are observed in pin-to-plane DC plasma systems where a liquid solution is used as a planar resistive anode. The size and structure of these patterns depends on the plasma current and salt concentration of the liquid anode. We propose that these patterns initiate due to the reaction and diffusion of electrons in the anode sheath, where electron impact ionization serves as an autocatalytic reaction. The resulting system of reaction-diffusion equations is amenable to Turing stability analysis, which we use to theoretically predict the transition from a uniform plasma to a ring-shaped pattern state. Expressing the stability criteria in terms of plasma current and solution salt concentration, we derive a theoretical phase boundary for the onset of pattern formation, which is in excellent agreement with experimental results.

Keywords: anode sheath, pattern formation, plasma-liquid interactions, anode spots

1. Introduction

A series of recent papers have shown remarkable images of radially symmetric patterns in DC discharges where the anode is a liquid (typically water) [1–6]. Interestingly, these patterns appear on an unbound, planar liquid surface, and the size of the features is largely independent of the system's geometric size, which is a common feature of Turing patterns [7, 8]. These liquid anode patterns are often considered a subset of the broader phenomenon of 'anode spots', which form when the space charge field reaches a critical value and begins to drive electron impact ionization in the anode sheath [9]. This effect has been demonstrated experimentally, theoretically, and in numerical simulations [10, 11]. The nonlinear coupling between the electric field and electron transport equation makes the mathematical analysis difficult, and additional nonlinearities arise when considering energy transport and temperature gradients in the anode sheath [13]. For liquid anodes, one must also consider the complex interactions between the plasma and liquid phase, which are not well understood [14]. Overall, the physical processes responsible for pattern formation on a plasma-liquid interface remain unclear.

Self-organized patterns also often appear in other types of low-temperature plasma, such as AC dielectric barrier discharges [12, 15–18] and DC glow discharges, usually with resistive electrodes [19–23]. A variety of reaction-drift-diffusion models coupled to electrostatics have successfully reproduced some of the observed features, such as temporal oscillations [24], striations [25, 26], radially symmetric patterns [27–29], and hexagonal lattices [12, 30]. However, most of these models are highly nonlinear and must be solved numerically. Thus, comparisons with experimental results are typically qualitative in nature, and it is often unclear what physical processes are essential for pattern formation.

As for the mechanism responsible for the patterns, it is widely believed that they arise from space charge accumulation near an electrode surface, while the specific geometric structure of a pattern depends on complex feedback mechanisms. For example, joule heating increases the gas temperature, which changes the density and the rate of ionization and diffusion. This type of thermal feedback mechanism typically results in hexagonal patterns [31]. Space charge created by ionization also changes the local electric field, resulting in a variety of different structures. In all the

[4] Author to whom correspondence should be addressed.

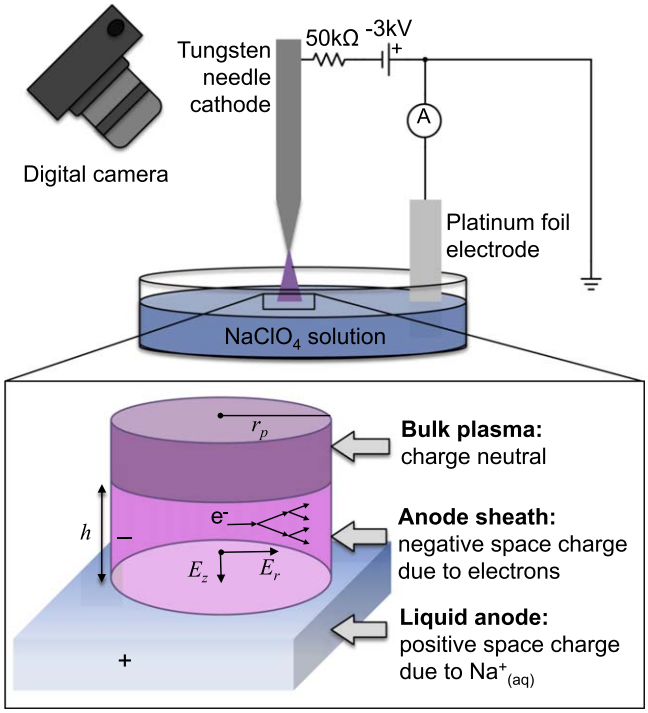

Figure 1. Schematic of the liquid anode DC glow discharge system used in this work. The inset on the bottom shows a close-up illustrating the electrostatics of the plasma-liquid interface. We postulate that an electron avalanche propagates radially outward, running parallel to the liquid surface.

complex processes and models that have been proposed, electron impact ionization and diffusion always appear as fundamental underlying processes. Thus, it has been postulated that the initial transition to a patterned state is due to a Turing reaction-diffusion instability, where electron impact ionization serves as an 'autocatalytic' reaction [32, 33].

In this work, we develop a simple theoretical model to predict the conditions for the onset of patterns on a liquid anode surface. Our model only considers the reaction and diffusion of electrons and ions and the basic electrostatics of the anode sheath, and it accurately predicts the phase boundary in terms of observable system parameters. The model is based on a Turing reaction-diffusion mechanism, where free electrons in the plasma phase serve as 'activators' with electron impact ionization being the autocatalytic reaction. The rate of ionization depends on the interfacial electrostatics of the anode sheath. Importantly, we posit that the radial space charge field E_r drives electron impact ionization, creating an avalanche running *parallel* to the liquid surface, as illustrated in figure 1. The radial space charge field E_r in the anode sheath increases with the plasma radius r_p, and the plasma radius is determined by the current and salt concentration of the liquid anode. Increasing the plasma current causes the anode sheath to expand radially outward, which causes the radial space charge field E_r to increase. At approximately 10 mA, the reduced electric field E_r/p reaches a critical value of approximately 100 Td, and electron impact ionization forms a ring pattern around the plasma boundary, which we confirm experimentally.

2. Experimental system

As shown in figure 1, discharges were formed in air by suspending a sharpened tungsten welding electrode (0.125 inch diameter) a distance of 3 mm above a sodium perchlorate ($NaClO_4$) solution. The gap distance was measured using a digital microscope (Dino-Lite USB Microscope) and set using a micrometer. A grounded piece of platinum (Pt) foil was submerged in the solution to serve as a counter electrode. The discharge was ignited by applying −3 kV DC (Power Designs INC., Model 1570) through a 50 kΩ ballast resistor to the cathode. The current I was measured using a digital multimeter (Amprobe AM-510) connected to the Pt foil counter electrode, and it was varied by adjusting the applied voltage. Plasma images were acquired using a Canon EOS Rebel T3i digital camera using exposure times of 1 or 5 ms, as noted below.

Sodium perchlorate solutions were prepared by dissolving an appropriate amount of $NaClO_4$ salt ($NaClO_4$, ACS reagent, ⩾98.0%, Sigma Aldrich) into de-ionized water to make batch solutions with concentrations of 8, 64, and 512 mM, which were further diluted to the desired concentrations. Aliquots of 80 ml of solution were poured into a 150 ml glass petri dish for all experiments.

3. Theoretical model

As patterns are confined to the anode sheath just above the liquid surface [4], we begin by considering the reaction and diffusion of free electrons $e^-_{(g)}$ and positive ions $A^+_{(g)}$ in humid air (either nitrogen $N_2{}^+_{(g)}$ or water vapor $H_2O^+_{(g)}$), where the radial electric field E_r drives electrons impact ionization

$$e^-_{(g)} + A_{(g)} \rightarrow 2e^-_{(g)} + A^+_{(g)}. \quad (1)$$

Electrons are lost by recombination

$$e^-_{(g)} + A^+_{(g)} \rightarrow A_{(g)}, \quad (2)$$

and dissociative electron attachment with water

$$e^-_{(g)} + H_2O_{(g)} \rightarrow H^-_{(g)} + OH_{(g)}. \quad (3)$$

In the language of Turing reaction-diffusion instabilities, reaction (1) serves as the autocatalytic reaction process with electrons as the activator, while reactions (2) and (3) are inhibitory processes that dissipate energy.

We consider the basic geometry shown in the inset of figure 1. To demonstrate that self-organized patterns are due to Turing's mechanism, we will neglect drift and assume the concentration of electrons n_e and ions n_i are governed by solely reaction-diffusion processes. The coupled reaction-diffusion equations in cylindrical coordinates are

$$\frac{\partial n_e}{\partial t} - D_e \nabla^2 n_e = \alpha \mu_e \overline{E}_r n_e - \beta n_e n_i - \gamma n_e \quad (4)$$

and

$$\frac{\partial n_i}{\partial t} - D_i \nabla^2 n_i = \alpha \mu_e \overline{E}_r n_e - \beta n_e n_i, \quad (5)$$

where D_e and D_i are diffusion coefficients, μ_e is the electron mobility, α is the Townsend coefficient for reaction (1), and β and γ are the rate constants for reactions (2) and (3), respectively. Equations (4) and (5) are subject to periodic boundary conditions in the azimuthal direction. We will also impose that the concentrations go to zero at the radial boundary of the plasma $r = r_p$. Additionally, recent simulation results from Bienek *et al* showed that patterns are confined to the anode sheath [28]. Accordingly, we impose a third Dirichlet boundary condition in the z-direction, where the concentration of both species goes to zero at the sheath boundaries, such that $n(z = 0) = n(z = h) = 0$, where h is the vertical height of the anode sheath. The sheath height is small, $h \sim 10\,\mu$m [1, 34], so the patterns are essentially confined to a very thin region above the liquid surface and appear as 2D patterns 'on the liquid surface'.

The radial electric field E_r determines the rate that electrons and ions are created, and it will be the bifurcation parameter that determines when patterns emerge. In previous work, we showed that an electrostatic double-layer forms at the plasma-liquid interface, where positive aqueous salt ions are drawn toward the surface, creating a region of positive space charge in the liquid phase that balances an equal and opposite amount of negative space charge in the plasma anode sheath region [35]. A similar structure was found in simulations by Gopalakrishnan *et al*, where $n_e \gg n_i$ in the anode sheath [34]. Thus, as a base case, we assume a uniform electron concentration $n_e = n_0$ and ion depletion with a concentration $n_i = 0$, such that the anode sheath is a uniform disk of negative space charge with height $z = h$ and radius $r = r_p$, as shown in the inset of figure 1. Within a uniform cylinder of charge, the radial electric field E_r increases linearly with r, and the average radial field is

$$\overline{E}_r \approx \left(\frac{qn_0}{4\varepsilon_0}\right) r_p, \tag{6}$$

where q is the charge of the electron and ε_0 is the permittivity of free space.

A common feature of low-temperature DC plasmas is that the plasma expands radially outward on the anode surface as current I is increased, such that current density $j = I/\pi r_p^2$ is constant [36], as shown in figure 3(right). Thus, the plasma radius is a function of current I and current density j

$$r_p = \sqrt{\frac{I}{\pi j}}. \tag{7}$$

Work by Verreycken *et al* shows that this relationship holds even for large, complex patterned states [2]. Additionally, due the electrostatics at the interface where the anode sheath is matched to the Debye layer in the liquid [35], the current density increases with the salt concentration or ionic strength I_S of the solution as

$$j(I_S) = j_\infty \frac{1 - \exp(-bI_S)}{\mathrm{erf}(\sqrt{bI_S})}, \tag{8}$$

where j_∞ and b are fitting parameters. Shown in figure 2, the current density for a 3 mm gap in air is plotted as a function of ionic strength for a sodium perchlorate ($NaClO_4$) solution used as an anode. The current was held constant around 8.4 mA, which is less than or equal to the critical value for significant pattern formation. At least ten photographs were taken of the plasma for a particular ionic strength. A Gaussian fit was applied to the radial intensity profile of the images, and the average Gaussian radius r_p was used to calculate the current density $j = I/\pi r_p^2$. (Further details on this technique can be found in [35].) Curve fitting equation (8) to the measured data yields $j_\infty = 2.56 \times 10^4$ A m^{-2} and $b = 0.027$ mM^{-1}.

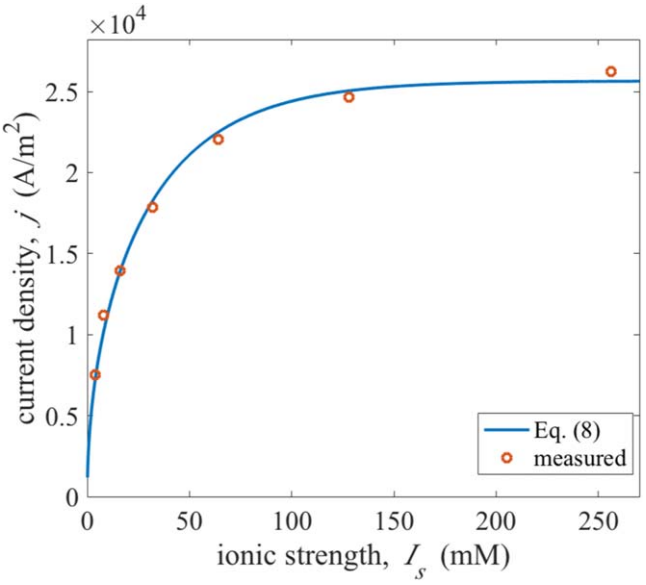

Figure 2. The current density measured as a function of the ionic strength of $NaClO_4$ solution for a 3 mm gap in air with a constant current of 8.4 mA. A sharpened 0.125 in. tungsten rod was used as a cathode. The solid line is a curve fit using equation (8).

All together, equations (6)–(8) show that the average radial electric field—which determines the rate of ionization—depends on both the plasma current, I, and the liquid solution ionic strength, I_S. A phase diagram can therefore be derived using linear stability analysis that will predict the critical values of I and I_S that yield a patterned state. Linearizing the rate of recombination about the quasi-equilibrium case $n_e = n_0$ and $n_i = 0$, such that $\beta n_e n_i \approx \beta n_0 n_i$, equations (4) and (5) can be written in linear matrix form as

$$\frac{\partial}{\partial t}\begin{bmatrix} n_e \\ n_i \end{bmatrix} - \nabla^2 \begin{bmatrix} D_e n_e \\ D_i n_i \end{bmatrix} = \begin{bmatrix} \alpha\mu_e \overline{E}_r - \gamma & -\beta n_0 \\ \alpha\mu_e \overline{E}_r & -\beta n_0 \end{bmatrix} \begin{bmatrix} n_e \\ n_i \end{bmatrix}. \tag{9}$$

The solution to equation (9) takes the form

$$\begin{bmatrix} n_e(\vec{r}, t) \\ n_i(\vec{r}, t) \end{bmatrix} = \sum_{l,m,n} \vec{u}_{lmn} \exp(\sigma_{lmn} t) Y_{lmn}(r, z, \theta), \tag{10}$$

where $\vec{u}_{lmn}$ is an eigenvector and σ_{lmn} is the temporal eigenvalue for a particular mode. Upon ignition, the plasma begins a superposition of various modes, which either grow or quickly decay depending on whether $\mathrm{Re}(\sigma_{lmn})$ is positive or negative. The modes are given by the eigenfunctions

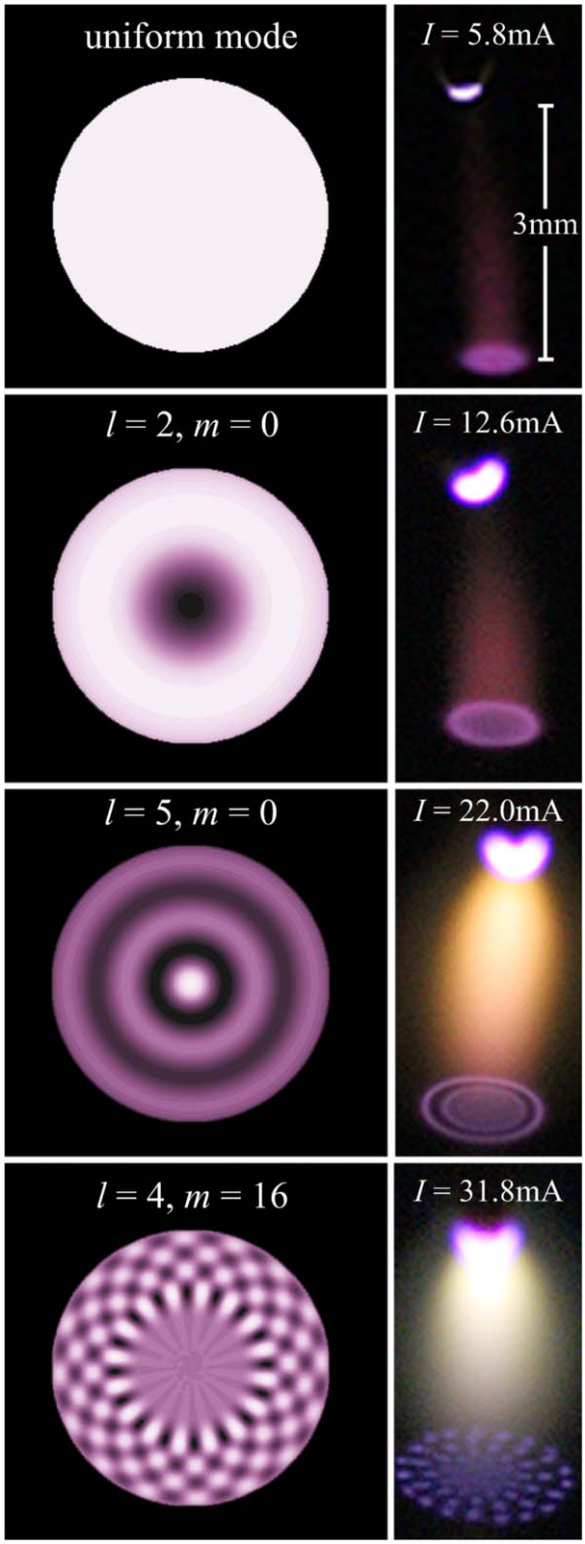

Figure 3. Shown on the left are the cylindrical harmonics given by equation (11) where $k_n z = \pi/2$. Shown on the right are photographs of patterns near the surface of an 8 mM $NaClO_4$ liquid anode solution in ambient air with a gap distance of 3 mm. Photographs were taken using an exposure time of 1 ms and have been contrast enhanced for clarity.

(harmonics) of the cylindrical Laplacian,

$$Y_{lmn}(r, z, \theta) = J_m(\kappa_{ml} r)[A_{ml} \cos(m\theta) + B_{ml} \sin(m\theta)] \sin(k_n z), \quad (11)$$

where $J_m(\kappa_{ml} r)$ is the mth Bessel function of the first kind. Note that the plasma has a finite radius r_p, which gives the boundary condition for the density of either species $n_{e,i}(r = r_p) = 0$. Thus, the radial eigenvalue becomes $\kappa_{ml} = a_{ml}/r_p$, where a_{ml} is the lth zero of the mth Bessel function. Importantly, the plasma radius r_p depends on current I and ionic strength I_S, as previously discussed.

Imposing the boundary condition $n_{e,i}(z = h) = 0$ ensures the pattern disappears in the bulk plasma [28]. The axial eigenvalue then becomes $k_n = n\pi/h$, where n is a positive integer. The 2-dimensional profiles of several modes given by equation (11) are shown in figure 2 (left), and they are remarkably similar to experimentally observed patterns (right).

The solution given by equation (10) is a separable product of temporal and spatial eigenfunctions with the properties $\partial_t e^{\sigma t} = \sigma e^{\sigma t}$ and $\nabla^2 Y_{lmn} = |k_{lmn}|^2 Y_{lmn}$, where $|k_{lmn}|^2 = \kappa_{ml}{}^2 + k_n^2$. Substituting equations (10) into (9) and replacing the differential operators with the scalars σ_{lmn} and $|k_{lmn}|^2$ yields the matrix eigenvalue problem

$$\sigma_{lmn}\vec{u}_{lmn} = \begin{bmatrix} \alpha\mu_e\overline{E}_r - \gamma - D_e|k_{lmn}|^2 & -\beta n_0 \\ \alpha\mu_e\overline{E}_r & -\beta n_0 - D_i|k_{lmn}|^2 \end{bmatrix}\vec{u}_{lmn}. \quad (12)$$

Note that the off diagonal terms have opposite sign, as one would expect for Turing patterns [7, 8]. For convenience, we will denote the matrix on the right-hand side of equation (12) as **A**.

A given mode Y_{lmn} becomes stable when the real part of its associated temporal eigenvalue $\mathrm{Re}(\sigma_{lmn}) = 0$. Equivalently, the $\mathrm{Re}(\sigma_{lmn}) = 0$ when the trace of the matrix in equation (12) is zero and its determinant is positive, or $\mathrm{tr}(\mathbf{A}) = 0$ and $\det(\mathbf{A}) > 0$. As $D_e \gg D_i$ [36], we can neglect the D_i term and it can be shown that $\det(A) \approx \gamma + D_e|k_{lmn}|^2$ is always positive, and the criteria for stability becomes

$$\alpha\mu_e\overline{E}_r - \gamma - D_e|k_{lmn}|^2 - \beta n_0 = 0. \quad (13)$$

Classically, the Townsend ionization coefficient α is related to the average electric field via [36].

$$\alpha = Ap \exp\left(\frac{-Bp}{\overline{E}_r}\right), \quad (14)$$

where p is the gas pressure and A and B are gas-dependent parameters determined either from experiment or by solving the Boltzmann equation with the appropriate cross sections. For this work, the parameters $\gamma = 10^8\ \mathrm{s}^{-1}$, $A = 1600\ \mathrm{torr}^{-1}\ \mathrm{m}^{-1}$ and $B = 36\,600\ \mathrm{V\,m}^{-1}\ \mathrm{torr}^{-1}$ were determined using the BOLSIG + Boltzmann solver [37] using cross sections from the Morgan database [38] for an admixture of 20% water, 64% nitrogen, and 16% oxygen, which corresponds to saturated water vapor in air above a liquid anode surface at approximately 60 °C [39]. A similar approach was used to determine the ionization parameters for krypton in [23].

Combining equations (6)–(8) and (14) and the eigenvalues $\kappa_{ml} = a_{ml}/r_p$ and $k_n = n\pi/h$, then substituting into the criterion for stability, equation (13), yields an implicit relationship between ionic strength I_S and plasma current I, which

Table 1. Parameters used in equation (15) to calculate the theoretical phase boundary in figure 4. The electron mobility is related to diffusivity via the Einstein relation $\mu_e = qD_e/kT_e$, where T_e is the electron temperature and k_B is the Boltzmann constant.

Parameter	Value
Electron number density, n_0	2.5×10^{18} m^{-3} [34]
Electron diffusivity, D_e	0.2 m^2 s^{-1} [37, 38]
Electron temperature, T_e	1 eV [37, 38]
Electron mobility, μ_e	0.2 m^2 V^{-1} s^{-1} [37, 38]
Anode sheath length, h	40 μm [1, 34]
Pressure, p	750 torr
Ionization parameter, A	1600 torr^{-1} m^{-1} [37, 38]
Ionization parameter, B	36 600 V m^{-1} torr^{-1} [37, 38]
Recombination rate const., β	10^{-13} m^3 s^{-1} [36]
Electron attachment rate, γ	10^8 s^{-1} [37, 38]

defines the phase boundary between patterned states,

$$Ap\exp\left(\frac{-4Bp\varepsilon_0}{qn_0}\sqrt{\frac{\pi j(I_S)}{I}}\right)\mu_e\left(\frac{qn_0}{4\varepsilon_0}\right)\sqrt{\frac{I}{\pi j(I_S)}} - \gamma - D_e\left(a^2{}_{ml}\frac{I}{\pi j(I_S)} + \frac{n^2\pi^2}{h^2}\right) - \beta n_0 = 0. \quad (15)$$

For a given ionic strength I_S, as the current I is increased, the first structured mode that satisfies equation (15) is the $l = 2$, $m = 0$ ring mode with $a_{02} = 5.52$. As the current is increased further, larger values of a_{ml} are required to satisfy equation (15), meaning that more complex, higher-order modes emerge. This is consistent with the experimental photos in figure 3 as well as those shown in [1–6]. In the next section, we will show that the phase boundary for the first ring mode predicted by equation (15) is consistent with our experimental observations.

4. Phase diagram and experimental validation

The implicit dispersion expression in equation (15) leads to a phase diagram identifying which values of I_s and I yield patterns. Shown in figure 5, a numeric root-finder was used to calculate the theoretical phase boundary (solid line) between spatially uniform modes and the $l = 2$, $m = 0$ ring modes. (Values used for the various plasma parameters are listed in table 1.) To validate the theory, the phase diagram was experimentally measured by photographing a liquid anode DC glow discharge in laboratory air for a wide variety of I_s and I conditions. For a given solution ionic strength I_S, the plasma current I was increased from 4 to 30 mA, and static photographs were analyzed in Matlab to determine if a ring structure was present. If the radial image intensity profile across the center of the plasma was clearly convex, it was deemed a ring pattern. (An example of the image analysis technique for $I_S = 256$ mM is shown in figure 4.) As shown in figure 5, conditions where either a uniform mode (closed circles) or a ring mode (open circles) were experimentally observed are in excellent agreement with the theoretical phase boundary predicted by equation (15).

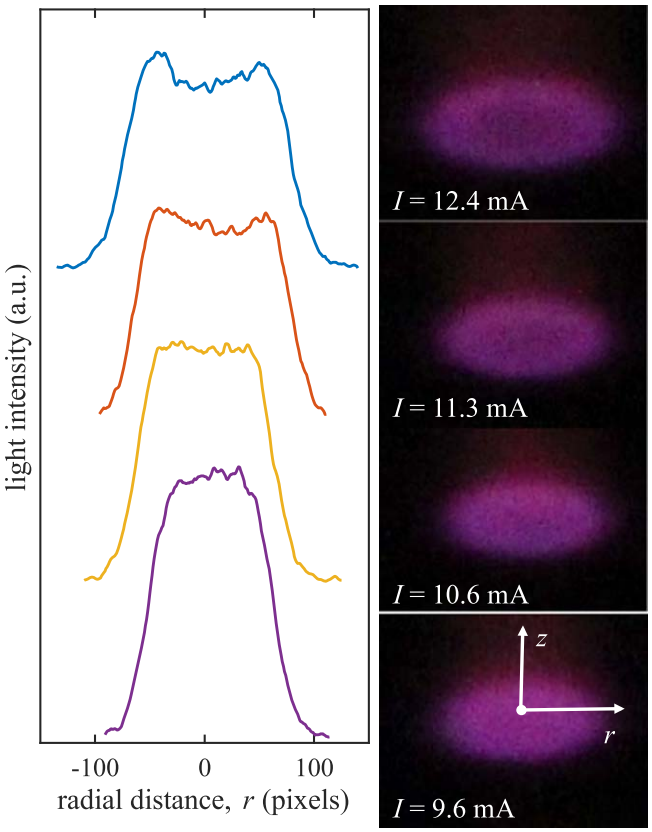

Figure 4. (Left) Radial intensity profiles, corresponding to the images on the right, are used to determine if a ring structure is present. The top two images have a clearly convex structure in the center, so they are deemed to contain a ring structure. (Right) Images of the anode sheath region at various currents for a liquid ionic strength of $I_S = 256$ mM.

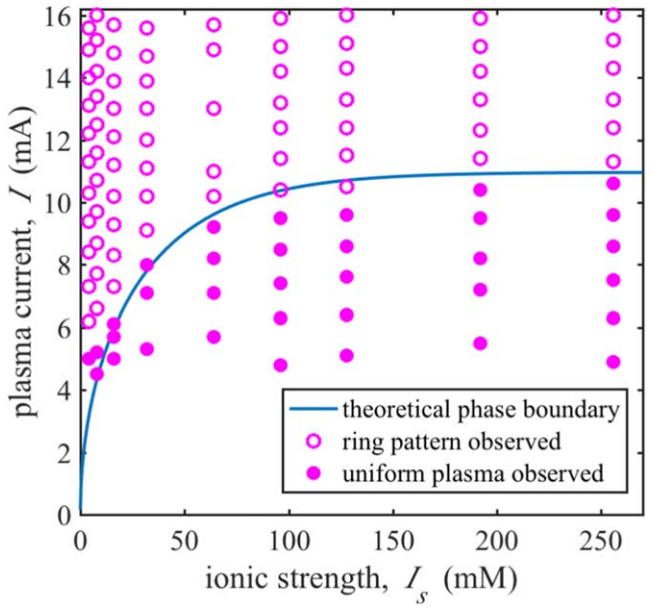

Figure 5. Measured phase diagram shows which control parameters yield ring patterns. The theoretical phase boundary is given by equation (15) with current density calculated using equation (8) and other parameters listed in table 1. Photographs were taken using an exposure time of 5 ms for the data shown here.

Turing patterns also feature an intrinsic wavelength that is not dictated by any boundary conditions, but rather by the reaction diffusion processes. Importantly, the size of rings and spots observed in this work and in [1–6] is independent of system dimensions, such as the gap distance and cathode diameter. In our model, the transition to a ring mode essentially occurs when the intrinsic wavelength matches the radial size of the plasma. The intrinsic wavelength or critical wavenumber can be determined by solving equation (13), yielding

$$|k_{lmn}| = \sqrt{\frac{\alpha\mu_e\overline{E_r} - \gamma - \beta n_0}{D_e}}. \tag{16}$$

For $I = 10$ mA and $I_S = 8$ mM, the critical wavenumber is $|k| \sim 10^5\,\mathrm{m}^{-1}$, which corresponds to a wavelength $\sim 100\,\mu$m. Again, this is approximately the size of the experimentally observed structures shown in figure 3 as well as those in [1–6], showing strong agreement between the theory and experimental observations.

5. Discussion and conclusions

Together, the theory and data show that simple patterns observed on a plasma-liquid interface are initiated by a simple reaction-diffusion mechanism with electron impact ionization serving as an autocatalytic reaction. The rate of ionization depends on the radial electric field in the anode sheath, which is dictated by the liquid ionic strength I_s and plasma current I. The analytically predicted phase diagram for the onset of patterns matches experimental observations well, and the model qualitatively predicts other observed features, such as the intrinsic wavelength and the shapes of higher-order modes at higher currents.

While our linear model accurately predicts the phase diagram for pattern onset, it is only valid for small mode amplitudes. At low currents, all pattern modes have a negative growth rate $\mathrm{Re}(\sigma_{lmn})$ and quickly decay to zero. As the current is increased, the growth rate of a particular mode $\mathrm{Re}(\sigma_{lmn})$ becomes positive. With a positive growth rate, electron and ion concentrations increase until the non-linearity of reaction (2) becomes significant, which likely results in unique temporal oscillations. References [1–6] report oscillations and rotations of the patterns at frequencies near 100 to 1,000 Hz. Our linear analysis predicts similar oscillations, but the calculated frequencies are much greater, $\mathrm{Im}(\sigma_{lmn}) \sim 10^6$ Hz, because it does not include the non-linearity of reaction (2).

Furthermore, our assumption of a uniform disk of space charge with $n_e = n_0$ and $n_i = 0$ and an average electric field clearly fails at higher plasma currents where the system progresses from the first ring-like mode to higher-order patterns. As a result, our simple model is unable to predict the observed progression of modes shown in figure 3. In our theory, every value of a_{ml} has a corresponding plasma current I and ionic strength I_S that will satisfy equation (15). However, many of these modes are not observed experimentally. For example, the observed pattern state shown in figure 3 abruptly transitions from the $l = 5$, $m = 0$ mode to a much higher-order mode with $m \approx 16$ as the current is increased. Recent simulations by Bieniek *et al* have shown that the spots in higher-order modes are regions of increased ion density with net positive space charge [28]. These spots serve as 'mini-cathodes' that locally attract electrons—an effect that is certainly not captured when we assume a uniform disk of negative space charge. There can be additional nonlinearities due to local gas heating in the individual spots [REFs]. The nonlinear feedback between ionization and the local electric field and gas density ultimately determines the structure of the higher-order modes after the system has transitioned to a patterned state. However, the initial transition can be accurately predicted by a simple reaction-diffusion model, as we have shown in this work.

Acknowledgments

The authors acknowledge useful discussions with J M Powers and D M Bartels. This work was supported by the US Army Research Office under Award Number W911NF-17-1-0119 and the National Science Foundation under Award Number NSF DMS 1516753.

ORCID iDs

Paul Rumbach https://orcid.org/0000-0002-0154-3045
David B Go https://orcid.org/0000-0001-8948-1442

References

[1] Bruggeman P, Liu J, Degroote J, Kong M G, Vierendeels J and Leys C 2008 *J. Phys. D: Appl. Phys.* **41** 215201
[2] Verreycken T, Bruggeman P and Leys C 2009 *J. Appl. Phys.* **105** 083312
[3] Shirai N, Uchida S, Tochikubo F and Ishii S 2011 *IEEE Trans. Plasma Sci.* **39** 2652
[4] Shirai N, Uchida S and Tochikubo F 2014 *Plasma Sources Sci. Technol.* **23** 054010
[5] Chen Z, Zhang Z, Levchenko I, Beilis I I and Keidar M 2017 *Sci. Rep.* **7** 12163
[6] Zhang S and Dufour T 2018 *Phys. Plasma* **25** 073502
[7] Turing A M 1952 *Phil. Trans. R. Soc.* **237** 37
[8] Cross M and Greenside H 2009 *Pattern Formation and Dynamics in Nonequilibrium Systems* (Cambridge: Cambridge University Press)
[9] Conde L, Ferro Fontán C and Lambás J 2006 *Phys. Plasma* **13** 113504
[10] Scheiner B, Barnat E V, Baalrud S D, Hopkins M M and Yee B T 2017 *Phys. Plasma* **24** 113520
[11] Scheiner B, Barnat E V, Baalrud S D, Hopkins M M and Yee B T 2018 *Phys. Plasma* **25** 043513
[12] Dong L, Shen Z, Li B and Bai Z 2013 *Phys. Rev.* E **87** 042914
[13] Raizer Y P and Mokrov M S 2013 *Phys. Plasma* **20** 101604
[14] Bruggeman P J *et al* 2016 *Plasma Sources Sci. Technol.* **25** 053002

[15] Ammelt E, Schweng D and Purwins H-G 1993 *Phys. Lett.* A **179** 348
[16] Gurevich E L, Zanin A L, Moskalenko A S and Purwins H-G 2003 *Phys. Rev. Lett.* **91** 154501
[17] Dong L, Mao Z, Yin Z and Ran J 2004 *Appl. Phys. Lett.* **84** 5142
[18] Stauss S *et al* 2013 *Plasma Sources Sci. Technol.* **22** 025021
[19] Donahue T and Dieke G H 1951 *Phys. Rev.* **81** 248
[20] Astrov Y A and Logvin Y A 1997 *Phys. Rev. Lett.* **79** 2983
[21] Ammelt E, Astrov Y A and Purwins H-G 1998 *Phys. Rev.* E **58** 7109
[22] Schoenbach K H, Moselhy M and Shi W 2004 *Plasma Sources Sci. Technol.* **13** 177
[23] Zhu W, Niraula P, Almeida P G C, Benilov M S and Santos D F N 2014 *Plasma Sources Sci. Technol.* **23** 054012
[24] Johnson J C, D'Angelo N and Merlino R L 1990 *J. Appl. Phys.* **23** 682
[25] Robertson H S 1957 *Phys. Rev.* **105** 368
[26] Rafatov I, Šijačić D D and Eber E 2007 *Phys. Rev.* E **76** 036206
[27] Trelles J P 2013 *Plasma Sources Sci. Technol.* **22** 025017
[28] Bieniek M S, Almeida P G C and Benilov M S 2018 *Plasma Sources Sci. Technol.* **27** 05LT03
[29] Bieniek M S, Santos D F N, Almeida P G C and Benilov M S 2018 *Phys. Plasma* **25** 042307
[30] Raizer Y P and Mokrov M S 2010 *J. Phys. D: Appl. Phys.* **43** 255204
[31] Mokrov M S and Raizer Y P 2018 *Plasma Sources Sci. Technol.* **27** 065008
[32] Purwins H-G and Stollenwerk L 2014 *Plasma Phys. Control. Fusion* **56** 123001
[33] Trelles J P 2016 *J. Phys. D: Appl. Phys.* **49** 393002
[34] Gopalakrishnan R, Kawamura E, Lichtenberg A J, Lieberman M A and Graves D B 2016 *J. Phys. D: Appl. Phys.* **49** 295205
[35] Rumbach P, Clarke J P and Go D B 2017 *Phys. Rev.* E **95** 053203
[36] Raizer Y P 1991 *Gas Discharge Physics* (Berlin: Springer)
[37] Hagelaar G J M and Pitchford L C 2005 *Plasma Sci. Sources Tech.* **14** 722
[38] Morgan database www.lxcat.net (Accessed: 8 April 2019)
[39] Moran M J and Shapiro H N 1998 *Fundamentals of Engineering Thermodynamics* (New York: Wiley)